ScienceDirect

Atmospheric Attenuation

Related terms:

Solar Radiation, Solar Energy, Extinction Coefficient, Wavelength, Aperture Area, Concentration Field, Concentrator

Detection of Explosives by Millimeter-wave Imaging

David M. Sheen, ... Thomas E. Hall, in Counterterrorist Detection Techniques of Explosives, 2007

4.6 Attenuation

Atmospheric attenuation, due primarily to water vapor absorption lines, is very significant in many spectral regions in the millimeter-wave and terahertz bands as shown in [56]. Most of the millimeter-wave band has relatively low losses over moderate path lengths, whereas frequencies above 1

THz suffer fairly extreme attenuation. There are a number of atmospheric windows in the spectral regions less than about 350 GHz, near 400 GHz, near 650 GHz, and near 850 GHz. Imaging systems operating away from these window regions will have very short ranges of operation because of the severe attenuation.

For some applications, various materials such as paper, cardboard, or clothing will need to be relatively transparent. Clothing samples have been measured and reported by Bjarnason et al. [1] whose results show that most clothing is reasonably transparent (i.e., one-way attenuation is less than about

6 dB) at frequencies less than about 600 GHz. The attenuation of various paper, cardboard, and fabric samples has been measured at PNNL. These results indicate that the paper samples are reasonably transparent (i.e., one-way attenuation is less than about 6 dB) at frequencies up to ~2 THz. The results from the fabric samples generally agree with those from Bjarnason et al., with losses generally low (typically < 3 dB) below 500 GHz and increasing markedly above 500 GHz.

In general, lower frequencies will offer improved penetration for most optical obscurants, creating a tradeoff between penetration and resolution that must be

considered when designing an imaging system for a particular application.

The Development of Solar Power Satellites

E. Glaser Peter, in Advances in Energy Systems and Technology, Volume 2, 1979

6 Microwave Beam Effects

a. Atmospheric Attenuation and Scattering (**Raytheon, 1975**). The atmospheric transmission efficiency of the microwave beam depends on meteorological conditions. Absorption by the atmosphere occurs when gaseous molecules with permanent dipole moments couple the electric or magnetic components of the microwave field to their rotational energy

levels. Most of the absorption due to excitation of collision-broadened lines occurs at the 22-GHz line of water vapor and 60-GHz line of oxygen.

Below 10 GHz the attenuation resulting from molecular absorption is approximately 0.1 dB or less, depending on the microwave beam elevation angle.

Attenuation of the microwave beam by rain, cloud droplets, snow, and hail will depend on their size, shape, and statistical distribution and composition. Rain, wet snow, melting precipitation, and water-coated ice attenuation is low at frequencies below 3 GHz. The most severe condition is expected in rain clouds, where attenuation may

reach 4% at 3 GHz. The attenuation produced by a 1-km path through wet hail could reach 13% at 3 GHz.

Forward scattering by rain and hail will increase the field intensity outside the main microwave beam. For example, a 5-GW SPS operating at 3 GHz would scatter 3 mW nearly isotropically if the storm cell height were 1 km. At a range of 10 km, the scattered microwave beam power density would be about 2×10^{-4} mW/cm^2. Therefore, scattering by rain or hail is not expected to increase sidelobe levels significantly or broaden the main microwave beam.

b. Ionospheric Propagation. Among the several possible

interactions of the microwave beam with the ionosphere are the following:

Ambient refraction of the microwave beam by the ionosphere. This effect leads to a negligible displacement. If horizontal gradients are present in the ionosphere, they could result in displacements (less than 100 meters) of the microwave beam (Raytheon, 1975).

Ionospheric electron density irregularities. These self-induced or ambient irregularities will cause phase fluctuations (less than 10 degrees) across the wave front of the reference beam propagated from the center of the receiving antenna to the transmitting antenna face.

Random phase variations will subside within a few hundred meters and within tens of seconds (Raytheon, 1975).

Power beam dispersion due to ionospheric density fluctuations will increase the field intensity at the beam edges by up to 30%. At low power densities these fluctuations at the edges of the beam will not cause any significant power loss (Raytheon, 1975).

Experiments at Platteville, Colorado, and Arecibo, Puerto Rico, indicated that microwave fluxes can produce significant changes in the thermal energy of the plasma in the D (*) (60-90 km), E (*) (90-150 km), and F (*) (150-340 km) regions. However, the direct

effect of microwave beam transmission with densities of 20-30 mW/cm^2 is likely to be small, inasmuch as the absorption at the 3-GHz frequency remains negligible, even with an order of magnitude increase in electron temperature and density. However, power densities greater than 100 mW/cm^2 could produce large horizontal electron density gradients that could cause significant beam displacement and dispersion. Results of recent experiments at Arecibo cast doubt that thermal runaway effects on the ionosphere will occur at these low microwave beam densities (Coco *et al.*, 1978). But thermal self-focusing and

plasma striations could occur; so the magnitudes of these effects will have to be determined analytically and experimentally.

Faraday rotation effects relating the total polarization twist of a linearly polarized wave to the total columnar electron content of the ionosphere under geomagnetically quiet conditions are projected to produce insignificant polarization losses. During geomagnetically disturbed periods— severe geomagnetic storms occur about three times a year—Faraday rotation and polarization loss is projected to be less than 1% (Raytheon, 1975).

PREDICTION OF ATMOSPHERIC PARAMETERS FOR SPECTRAL AND TOTAL SOLAR IRRADIANCES

Hamdy M. Shafey, in Energy Developments: New Forms, Renewables, Conservation, 1984

Atmospheric Parameters

The sources of the atmospheric attenuation mentioned above depend on the considered site, and they are mainly influenced by the following parameters. (16)

1. The constant C_R for the inverse fourth power law dependence of Rayleigh scattering coefficient on the wavelength.
2. The ozone (O_3) equivalent layer thickness L at normal pressure and temperature.
3. The empirical Ångström coefficient β and the

wavelength exponent γ for the extinction coefficient of the Mie scattering and absorption.

4. The water vapor (H_2O) content represented by a liquid-layer thickness w.

The terrestrial direct spectral solar irradiance F_b, λ can be expressed as the extraterrestrial value F_O, λ reduced by a spectral atmospheric attenuation function yλ which includes these five parameters and depends on the air mass ratio m as follows.

$$F_{b,\lambda} = F_{0,\lambda} y_{\lambda}(C_R, L, \beta, \lambda, w, m) \quad (6)$$

The equation by Watt (15) is adopted for the calculation of m.

Following Thekaekara (18), the

function yλ can be written for both visible and infrared regions of the wavelength as

$$y_\lambda = T\ \exp\{-(C_{1,\lambda}+C_{2,\lambda}L+C_{3,\lambda})m-(C_{4,\lambda}+C_{5,\lambda})\sqrt{wm}\}, \quad (7)$$

$$T = 1 - C_{6,\lambda}\sqrt{m}, \quad (8)$$

$$C_1,\lambda = C_R/\lambda^4, C_3,\lambda = \beta/\lambda^\gamma, \quad (9)$$

where $C_{2,\lambda}$, ($C_{4,\lambda}$, + $C_{5,\lambda}$) and $C_{6,\lambda}$ are known spectral coefficients of band absorption by O_3, H_2O and CO_2 respectively. (18)

Broadband radio-over-fiber technologies for next-generation wireless systems

Jianjun Yu, ... Xiaodan Pang, in Optical Fiber Telecommunications VII, 2020

22.2.1 Basic photonic up-conversion schemes

Due to the high free-space loss and atmospheric

attenuation of mm-wave signals, the coverage of each radio transmitter is reduced to tens to hundreds of meters, which means that a large number of BSs are required to provide a wide geographic coverage [16]. Therefore a low-cost simplified BS design is critical to the commercialization of the fiber-optic wireless hybrid networks with mm-wave links. To carry high-speed wireless data, it is necessary to generate and transport mm-wave signal with high transmission power, high bandwidth and high phase noise tolerance. High frequency RF sources, mixers, or cascaded frequency multiplexers [17,18] are

commonly required to generate mm-wave signals using an electrical up-conversion method. This method can usually satisfy the requirements of phase noise and power performance of the generated signal. However, given the trade-off between further expansion of signal bandwidth and increased system complexity, this approach is not considered the best solution in the long run.

On the other hand, using photonic technology to generate wireless signals has the advantage of broad bandwidth that can be achieved by opto-electronic devices. The principle of this method is photonic heterodyne mixing [16,19,20].

Various techniques for generating mm-wave signals have been proposed, and they can usually be divided into two basic categories. The first uses coherent laser sources for heterodyne mixing, which can be achieved by using Mach–Zehnder modulator (MZM) [21], dual-mode distributed feedback laser [22], subharmonic mode-locked laser [23,24] or optical frequency comb. Fig. 22.7 shows three typical coherent up-conversion schemes using single wavelength lasers to realize photonic wireless communication links, among many others.

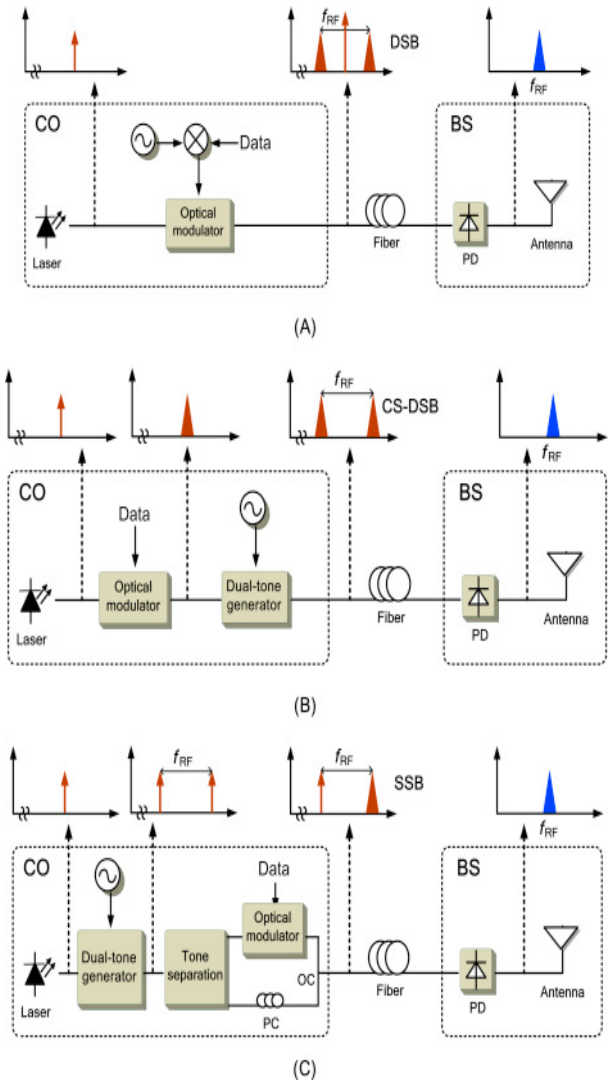

Figure 22.7. Millimeter-wave (mm-wave) generation schemes based on a single optical source. (A) Scheme A, (B) scheme B, and (C) scheme C. *CO*, Central office; *BS*, base station; *CS-DSB*, carrier suppressed-double sideband; *SSB*, single sideband; *PC*, polarization controller; *OC*,

optical coupler.

Scheme A is similar to a traditional double-sided band (DSB) RoF system in which data is first modulated onto an RF carrier before being fed to optical modulator. The difference is that the carrier suppression-DSB (CS-DSB) scheme is used to eliminate periodic RF power fading caused by dispersion in optical fibers and reduces half of the RF source demand [25]. Similarly, CS-DSB modulation technology is employed in scheme B. In this scheme, instead of modulating the data to the RF carrier, the data is directly modulated to the lightwave to form an optical baseband signal, which is then

fed to the dual-tone generator for frequency conversion. By doing so, the bandwidth limitations of RF devices such as mixers can be eliminated. The frequency of optical mm-wave signals is doubled by the CS-DSB scheme, so we can reduce the bandwidth requirement for optical and electrical devices [25]. Both schemes A and B support amplitude modulation formats, such as on-off keying and pulse amplitude modulation signals. However, since both the upper and lower bands contain modulated signals, heterodyne mixing with common square-law detection will result in the loss of phase information. Therefore they

are not suitable for complex signal formats containing phase modulation, such as phase shift keying, orthogonal amplitude modulation (QAM), and complex valued orthogonal frequency division multiplexing (OFDM) signals. Researchers have made several efforts to adapt to systems that transmit complex signals. In scheme A, by converting the baseband signal to IF signal before mixed with RF signal, after heterodyne jitter, the converted complex signal can be removed from the frequency component generated by the sideband which contains data, or so-called “jitter noise”, so that the intensity and phase information can be reserved

[26]. Different from scheme A and B, scheme C separates the upper and lower bands after the two-tone generator, as shown in Fig. 22.7. The data is modulated to one sideband and the other sideband is used as the carrier signal. In this scheme, the signal and carrier are combined together to form a single sideband (SSB) RoF signal before transmission over the fiber link, thus it can preserve the complex signal format after heterodyne mixing and eliminate the RF power fading effect in the fiber. Since the modulated signal by the optical modulator is a baseband signal and the optical modulator has a bandwidth up to 40 GHz, we

can generate very large bandwidth RoF signals by this scheme. The mm-wave signals generated by the schemes A, B and C based on a single external modulator have a stable frequency [27–32].

Fig. 22.8 shows another two schemes (schemes D and E) [27–30,33], where the two independent lasers run freely without frequency locking. By changing frequency spacing between the two lasers, the mm-wave signals at any frequency after heterodyne beating in a photodiode (PD) can be generated. But the generated mm-wave signals have a frequency instability problem since the two independent lasers used for heterodyne beating are not

frequency-locked [33,34]. In scheme D, the continuous-wave (CW) lightwave and the modulated lightwave are generated at the CO, so the BS has no laser source, which makes it simple. In scheme E, the CW laser locates in the BS. This scheme can be used to realize polarization multiplexing mm-wave signal generation [33], and it is employed to demonstrate large-capacity mm-wave signal generation with multidimensional multiplexing. Moreover, the optical signal generated at the CO is a baseband signal, and we can easily realize over 100-km fiber transmission from the CO to the BS.

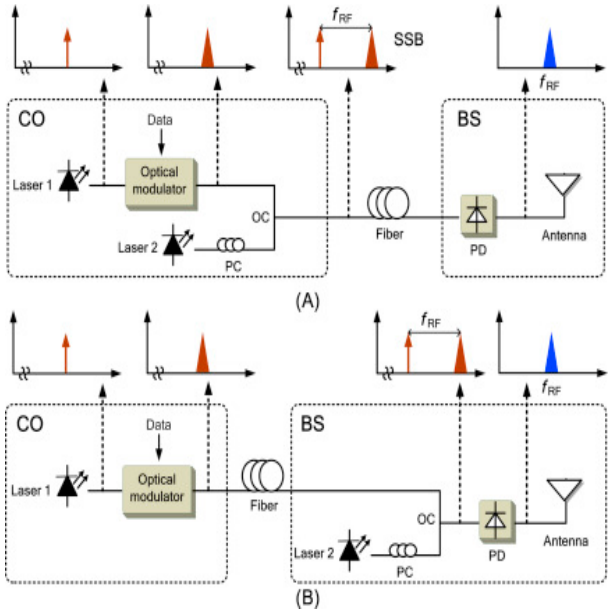

Figure 22.8. Millimeter-wave (mm-wave) generation schemes based on two free-running lasers. (A) Scheme D and (B) scheme E.

As each of the aforementioned five basic photonic up-conversion schemes has its own limitations, there is an improved scheme to generate optical mm-wave signal based on the external modulator [27,28]. This scheme simplifies the system structure and

reduces the cost because only one laser source and one modulator are used. In addition, mm-wave signals can carry different types of modulation formats, including single carrier and multicarrier OFDM. Since OFDM usually has arbitrary amplitude and phase, the processing for OFDM vector signal generation will be different from that for single-carrier vector signal generation. We will discuss separately how to generate vector QAM mm-wave signal based on the two different modulation formats in the following section.

Solar Thermal Systems: Components and Applications

B. Hoffschmidt, ... O. Kaufhold, in Comprehensive Renewable Energy, 2012

3.06.4.4.1 Receiver efficiency and optical and thermal losses

The heliostat field concentrates the solar beams onto the receiver. Not all of the radiation reaches the surface. Atmospheric attenuation and intercept appear on the way to the receiver as well as spillage losses. Spillage occurs due to dilution of light at the surface and is derived from the effects of a finite solar heliostat and various errors inherent in optical hardware and control of the heliostat field. Further, not all of the radiation is absorbed due to the reflectivity ratio of the receiver material. **Figure 27** displays the

different loss mechanisms at the receiver.

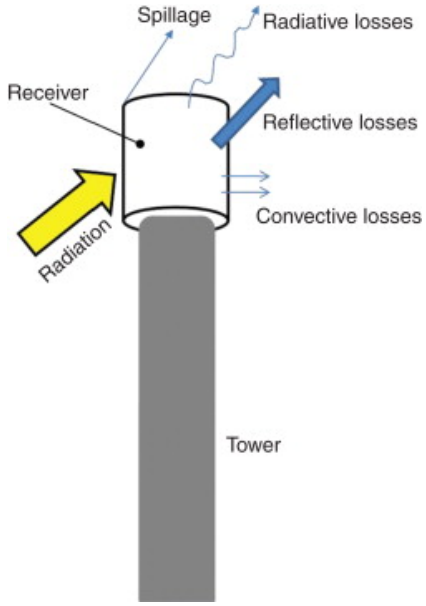

Figure 27. Energy balance of a solar receiver.

Wind velocity induces forced convection at the absorber surface. Also natural convection appears, which is dependent on the ambient temperature.

In addition to convection, radiation from the receiver to ambient contributes largely to thermal loss, according to

Stefan–Boltzmann equation. The final heat loss term represents the heat conducted away from the receiver. Most of this heat is lost through the receiver-supporting components that connect the receiver to the tower structure.

Thermal losses also take place by heat transport of the HTF via pipes to the steam recovery heat generator.

Receiver efficiency η_{rec} may be defined as described in Reference 56 as the product of each loss mode efficiency:

$$\eta_{rec} = \eta_{sp}\eta_{abs}\eta_{rad}\eta_{conv}\eta_{cond} \quad [5]$$

where η_{sp}, η_{abs}, η_{rad}, η_{conv}, and η_{cond} are efficiencies based on receiver spillage, absorption, radiation, convection, and conduction

losses, respectively.

Oil Spill Remote Sensing

M. Fingas, C.E. Brown, in Oil Spill Science and Technology (Second Edition), 2017

5.2 Atmospheric Properties

The atmosphere has certain transmission/adsorption windows that affect the way that one can carry out remote sensing. Figs. 5.1–5.3 show the atmospheric attenuation at different electromagnetic wavelengths. These figures show that the commonly used wavelengths in the visible, long-wave infrared, and radar bands are relatively free of atmospheric adsorption. One must consider rain, fog, and snow, which limit operations

in both the visible and the infrared regions. This leaves radar as the only all-weather and day-and-night sensor. Radar, as noted below, has many limitations in that it does not actually detect oil but only detects the dampening of sea capillary waves at a certain range of wind speeds.

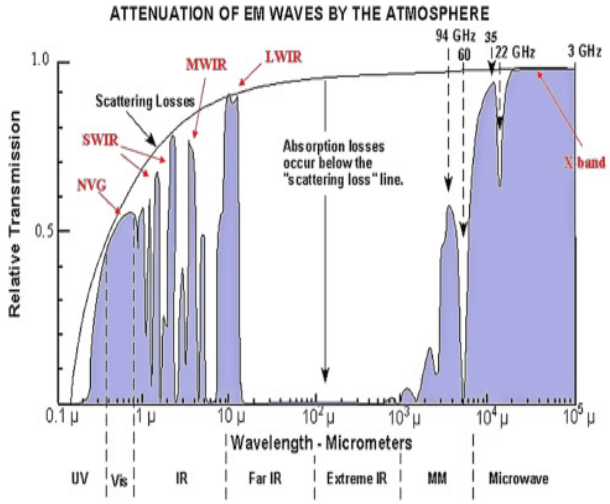

Figure 5.1. Atmospheric attenuation in the electromagnetic spectrum. *EM*, electromagnetic; *IR*, infrared; *LWIR*, longwave infrared; *MM*, millimeter; *MWIR*, medium wave infrared; *NVG*, Night-Vision Goggle area; *SWIR*, short wave infrared; *UV*, ultraviolet; *Vis*, visible.

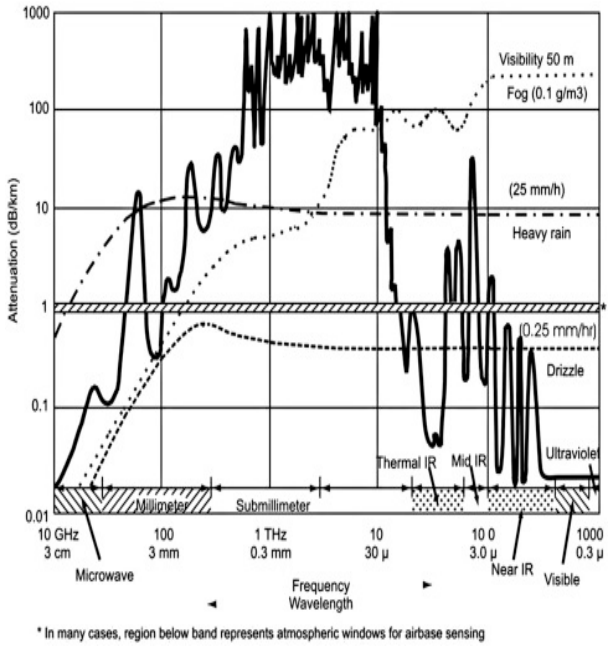

Figure 5.2. Another view of atmospheric attenuation.

Figure courtesy of Ron Goodman.

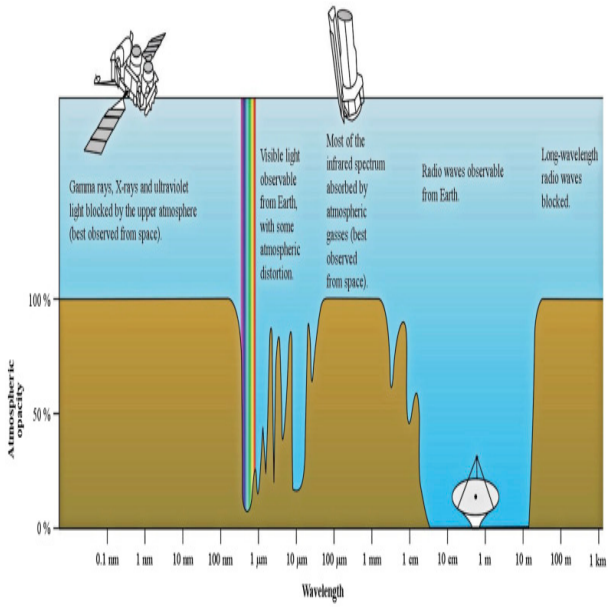

Figure 5.3. Atmospheric attenuation from a remote sensing point of view.

Systems and Applications

NICHOLAS FOURIKIS, in Advanced Array Systems, Applications and RF Technologies, 2000

1.6.2.2 Atmospheric Attenuation

The attenuation experienced by EM waves from atmospheric gases, rain, and fog as a function of frequency is documented in many references (e.g. [67]). For a given site, the attenuation experienced by EM waves at the resonant frequencies of O_2, and H_2O is significant and depends on the height of the site above sea level.

The approximate atmospheric attenuation experienced by EM waves in clear weather and during light and heavy rain conditions at 10, 35, 94 and

140, GHz is shown in Table 1.8 [68]. Designers have to accept the free-space attenuation of the EM waves as well as the attenuation caused by scattering during periods of rainfall. The attenuation of EM waves caused by depolarization is recoverable, however, and we shall further consider the effects of rain on polarimetric radar and satellite communication systems in section 1.6.12.2.

Table 1.8. Attenuation factor α (dB/km) as a function of weather conditions and frequency

Conditions	Frequency [GHz]			
	10	35	94	140
Clear weather	0.05	0.11	0.44	1.8
Light rain, 10 mm/h	0.133	2.6	8.7	5.9
Heavy rain, 25 mm/h	0.385	6.50	12.55	

While communication and radar systems usually operate at frequency bands for which the atmospheric attenuation is minimal, e.g. 30–40 and 80–100 GHz, short-range secure communications and radar systems operate at frequency bands for which the atmospheric attenuation is high, e.g. 22 and 60 GHz. Knowledge of the magnitude of attenuation due to rain and the atmosphere at the designated frequency of operation of a system serves the purpose of setting safe operational margins.

More detailed studies of the many influences of rain on the propagation of EM waves have been undertaken by the millimeter-wave radar and

satellite communications communities [68,69]. Estimates and measurements of the same attenuation under conditions of snowfall and fog have also been collated in reference [68].

Tropospheric impairments: Measurements and mitigation

Rajat Acharya, in Satellite Signal Propagation, Impairments and Mitigation, 2017

7.2.1.6 Combining the effects

The net fade distribution due to tropospheric refractive effects, $A_T(p)$, is the combination of various component factors like the rain fade, cloud attenuation, gaseous absorption and other effects described above. For

systems operating at frequencies above about 18 GHz, and especially those operating with low elevation angles and/or low margins, the effect of multiple sources of simultaneously occurring atmospheric attenuation must be considered very critically as the link quality and sustainability is sensitive to even smaller variations. The estimation of total attenuation due to multiple sources of simultaneously occurring atmospheric attenuation can be done by knowing the individual attenuation values for the required time percentage of occurrences. Let, A_G (p) be the gaseous attenuation due to water vapour and oxygen for a fixed

exceedance probability of p expressed in dB. Also, let $A_R(p)$ be the attenuation due to rain, $A_C(p)$ be the attenuation due to clouds and $A_S(p)$ be the fade due to tropospheric scintillation, all estimated for the same fixed exceedance probability p. Then considering the mutual dependence of different factors, we get the combined attenuation as

$$A_T p = A_G p + A_R p + A_c p^2 + A_s^2 p^{½} \tag{7.50}$$

where p is the probability of the attenuation being exceeded in the range 50%–0.001%. For percentages of time lower than 1%, the cloud and the gaseous attenuation is capped to their 1% occurrence probability

value.

Detection of Explosives by Terahertz Imaging

John F. Federici, ... Zoi-Heleni Michalopoulou, in Counterterrorist Detection Techniques of Explosives, 2007

3.2 Close range versus standoff detection

Several of the THz imaging methods described above have shown promise for THz security screening. Imaging of concealed weapons can be roughly classified by the effective range of the imaging. Close range (< 3 m) imaging offers solutions to a wide variety of applications. Over short distances, atmospheric attenuation and scattering is minimal. Screening of mail, packages, and baggage is a

close range application, whereas detection of explosives, weapons, and illicit drugs on people approaching a checkpoint or portal are a standoff application. Standoff (> 3 m) THz imaging allows for long-range screening and detection and potentially offers a solution for scanning persons in open areas such as airports, stations, etc. As discussed below, the range requirements partially determine the architectural choices of the detection system.

New methods and instruments for performance and durability assessment

M. Röger, ... F. Sutter, in The Performance of Concentrated Solar Power (CSP) Systems, 2017

7.2.1.5 Simulations supported by measurements

Today's raytracing simulation codes yield very accurate solar flux distribution results. An example is shown in Fig. 7.11. The accuracy of the results depends mainly on the quality of input parameters, such as correct representation of concentrator contour errors (slope errors), heliostat tracking errors, heliostat positions and geometry (blocking and shading, cosine effects, optical aberration), mirror reflectivity, atmospheric conditions (DNI, sunshape, atmospheric attenuation), tower geometry (shading), and

receiver position. The validity of the simulated flux maps should be confirmed by a measurement [47].

During the tests of a solar-hybrid gas turbine system at the Plataforma Solar de Almería [58], raytracing simulation results were compared to flux maps produced with a moving bar target. The raytracing code STRAL [46,50] is used. The heliostat contour error input is derived by deflectometry [41]. A major issue is to use correct aim points in the simulations because the used version of the heliostat control software has not always worked without errors. A random tracking error of having a sigma of about 0.9 mrad for each axis is

assumed. Fig. 7.13(a1) shows the simulated flux distribution on the radiation shield plane. The receiver aperture indicated by the black circle intercepts 266 kW.

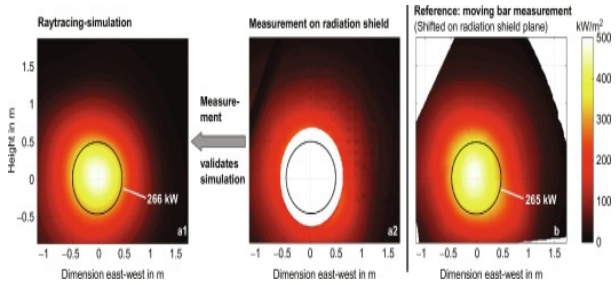

Fig. 7.13. Flux maps on radiation shield plane in kW/m^2 (PSA, 46 heliostats): (a1) Raytracing simulation; (a2) measurement directly on radiation shield (after application of correction matrix and calibration); and (b) moving bar reference measurement shifted to radiation shield plane.

The simulation is compared

with a flux measurement, using a CCD camera and the white radiation shield mounted around the aperture surface as a target; see Fig. 7.13(a2). Usually, the radiation shield is not perfectly white and not perfectly Lambertian. A correction matrix is applied to the gray value images to correct for spatial variations in reflectance. The calibrated flux distribution on the radiation shield is shown in Fig. 7.13(a2).

The standard deviation between the simulated and measured flux distribution on the radiation shield indicates the quality of the simulation of the flux distribution. The mean deviation gives information about the quality

of calibration of the measurement and the raytracing input parameters influencing power like heliostat reflectivity, DNI, or atmospheric attenuation. Various simulations with statistically varied heliostat aim points are done, and the one with the lowest deviation to the measurement is taken. Another possibility to validate the simulations is using distributed flux gauges in the receiver aperture. This variant may be especially valuable for large-area receivers with multiaim-point strategy and relative small reflection shield surface around the receiver. The validated simulation is taken to evaluate the flux on the aperture surface and the

power integrated over the aperture (266 kW). The reference input power of the moving bar measurement (generally not available, Fig. 7.13(b)) is 265 kW. Other measurements suggest a measurement uncertainty for the setup at the PSA in the range of about ± 2% compared to a moving bar measurement [47].

In Ref. [59], the measurement-supported technique is applied to measure the solar input power of a 3.1 MW_{th} tubular pressurized solar gas demonstration receiver in the SOLUGAS project. Here, a measurement uncertainty of the solar input power between – 1.3% and + 6.3% is achieved. As no mechanical

parts are involved, the measurement-supported simulation technique has high reliability, low susceptibility to loads and environment, low costs, and low complexity but need good knowledge about tracking accuracies and real heliostat aim points to achieve low uncertainties.